Elasticity of frictionless particles near jamming

Kamran Karimi and Craig E. Maloney

Phys. Rev. E **92**, 022208 — Published 21 August 2015

DOI: 10.1103/PhysRevE.92.022208

Elasticity Of Frictionless Particles Near Jamming

Kamran Karimi[1,*] and Craig E. Maloney[1,†]
[1] *Carnegie Mellon University, Pittsburgh, PA 15213*

We study the linear elastic response of harmonic disc packings near jamming via three types of probes: i) point forcing, ii) constrained homogeneous deformation of sub-regions of large systems, and iii) unconstrained deformation of the full system subject to periodic boundary conditions. For the point forcing, our results indicate that the transverse component of the response is governed by a lengthscale ξ_T which scales with the confining pressure, p, as $\xi_T \sim p^{-0.25}$, while the longitudinal component is governed by ξ_L which scales as $\xi_L \sim p^{-0.4}$. The former scaling is precisely the transverse lengthscale which has been invoked to explain the structure of normal modes near the density of states anomaly in sphere packings, while the latter is much closer to the rigidity length, $l_* \sim p^{-0.5}$, which has been invoked to describe the jamming scenario. For the case of constrained homogeneous deformation, we find that $\mu(R)$, the value of the shear modulus measured in boxes of size R, gives a value much higher than the continuum result for small boxes and recedes to its continuum limit only for boxes bigger than a characteristic length which scales like $p^{-0.5}$, precisely the same way as l_*. Finally for the case of unconstrained homogeneous deformation, we find displacement fields with power spectra which are consistent with independent, uncorrelated Eshelby transformations. The transverse sector is amazingly invariant with respect to p, and very similar to what is seen in Lennard-Jones glasses. The longitudinal piece, however, is sensitive to p. It develops a plateau at long wavelength, the start of which occurs at a length which grows in the $p \to 0$ limit. Strikingly, the same behavior is observed both for applied shear and dilation.

PACS numbers:

I. INTRODUCTION

For many years now, it has been known that packings of elastically deformable particles, confined by a compressive external hydrostatic pressure, exhibit an anomalous elastic response near the limit of zero confining pressure, p [1–3]. Mason and Weitz first observed this experimentally in sheared emulsions where the low frequency linear elastic storage modulus showed a sharp transition by many orders of magnitude as the volume fraction of the particles, ϕ, crossed the nominal random-close-packing volume fraction, ϕ_c [4]. This result generated many theoretical, numerical, and experimental studies over the next decade (for a review, see reference [5]).

A seminal numerical study by O'Hern et al. [1] showed that in a simple, frictionless disc/sphere packing model, the shear modulus vanished as ϕ went to its critical value, ϕ_c, while the compression modulus remained finite. Several later works related this anomalous vanishing of the shear modulus to an excess of low energy, "floppy", eigenmodes below an energy scale, ω_*^2, that vanished as $\phi \to \phi_c$ [6, 7]. However, the relationship between the energy scale at which these floppy modes appear and various lengthscales associated with them and the elastic response of the system has remained more subtle. This is problematic as understanding the elastic response is crucial for formulating a comprehensive theory of the mechanical response of these systems at larger strains and finite rates.

Much of the early work connecting the vanishing of ω_* to the emergence of diverging characteristic lengths neglected the role of quenched stresses in the contact network [8–10]. Within this stress-free context, it was generally agreed upon that there was one length scale associated with rigidity, l_* [8], and another length associated with the structure of the eigenmodes at the ω_*^2 energy scale, l_T. In particular, Xu et al. [11] showed that there was a change in eigenmode character at the anomaly in the density of states. Silbert et al. [12] did include the effects of quenched stresses and were able to show that the transverse power of the normal modes at ω_* peaked at a wave-vector with a length-scale, ξ_T that grew roughly as $p^{-0.25}$. They argued that an analogous measurement for the longitudinal power would show a ξ_L that would scale in the same way with $\delta\phi$ as ω_*^{-1} but were unable to demonstrate this numerically.

More recently, Lerner and co-workers [13] have shown, in a repulsive soft-disc system that the elastic response to a point perturbation is governed by l_T. This result seemingly contradicted earlier work by Ellenrboek and co-workers [10] who showed that the point response (also in models including the effect of the quenched forces) is controlled by l_* rather than l_T. One of the central results of the present work reconciles these two viewpoints.

We show that the longitudinal contribution to the point response is much more sensitive to pressure with an associated length $\xi_L \sim p^{-0.4}$ (close to the $l_* \sim p^{-0.5}$ result), and the transverse contribution is much less sensitive to pressure with $\xi_T \sim p^{-0.25}$ (completely analogous to l_T scaling). However, the overall point response is predominantly transverse at jamming (the ratio of shear to compression modulus goes to zero at jamming), so in

*Present address:Université Joseph Fourier, Grenoble, France
†Present address:Northeastern University. Boston, MA 02115

analyses that do not carefully separate longitudinal from transverse, the dominant effect will come from ξ_T and one would observe a length growing like $p^{-0.25}$.

We also probe the local elastic modulus by imposing homogeneous shear using no slip boundary conditions with boxes of various size, R. The rigid constraints imposed at the walls squelch non-affine relaxations and raise the value of shear modulus beyond its fully relaxed value. We find that the constrained shear modulus recedes to its limit as $\mu(R)/\mu_\infty - 1 \sim p^{-0.5}R^{-1}$. This is consistent with l_* governing the shear modulus in finite regions driven with no-slip boundary conditions and is analogous to the findings of During *et. al.* on pinning effects in diluted spring networks [14]. Physically this means that the size of the sample one needs to obtain a well-converged measure of the true relaxed shear modulus diverges at jamming.

Finally, we study the unconstrained response to global, homogeneous strain (both volumetric and shear) using periodic boundary conditions. The power spectrum of the response is similar to previous reports on Lennard-Jones [15, 16] glasses where it was shown that $|u(q)|^2 \sim q^{-2}$ but with important details not observed before and some interesting sensitivity to jamming. In particular we show that, under imposed shear, both transverse and longitudinal power have an anisotropic form. In real space, the shear response appears to be dominated by a few strong displacement quadrupoles reminiscent of Eshelby transformations aligned with the globally imposed shear. Under imposed global dilation/compression, the transverse and longitudinal power are anisotropic on average, but, like the shear response, are dominated by a few strong localized displacement quadrupoles in real space which generate strong local anisotropy. As $p \to 0$, very surprisingly, the transverse power spectrum remains largely unchanged in both shear and dilation! The longitudinal power spectrum, on the other hand, for both applied shear and applied dilation, shows a pronounced p sensitivity. It develops a characteristic feature at short wavelength that intensifies as $p \to 0$. The coherent shear zones, still visible in the transverse field near $p = 0$, become essentially incoherent zones of local dilation/expansion in the longitudinal piece with no coherent organization of the dilatancy field as at higher p. At longer wavelength, there is a minimum in the power which goes to increasingly longer wavelengths as $p \to 0$. For the system sizes studied here, it is difficult to describe this growing length with precision, but it is not inconsistent with the rigidity length, l_*.

The rest of this paper is organized as follows. In Section II, we describe our model and numerical protocols. In Section III, we discuss the response to a point force. Section IV discusses the response to homogeneous deformation with no slip boundary conditions, and recalls how one computes the elastic moduli using linear response theory. In Section V, we describe the response to homogeneous deformation of the full system with periodic boundary conditions.

II. MODELS AND SIMULATION PROTOCOLS

We perform simulations of frictionless granular packings in a periodic, two-dimensional cell subject to an isotropic pressure. The packings consist of N particles and a well studied binary mixture [1]: $N_A/N_B = 1$, $d_A/d_B = 1.4$, d is the diameter of the species. The position of the i-th particle is described by $\mathbf{r}_i$. Note that we use the convention that Latin letters refer to particle indices. We use bold type or Greek indices to refer to Cartesian vectors and sum over Greek indices implicitly. The particles interact via a pairwise, repulsive, central potential $U(r_{ij}) = \frac{1}{2}k_{ij}\delta_{ij}^2$ for $\delta_{ij} > 0$ and zero otherwise where k_{ij} is the spring constant, δ_{ij} is the overlap between the particles, $\delta_{ij} = d_{ij} - r_{ij}$, where $d_{ij} = \frac{1}{2}(d_i + d_j)$, and r_{ij} is the distance between the particles. $U(r_{ij})$ can be alternatively defined as $U(s_{ij}) = \frac{1}{2}\varepsilon s_{ij}^2$ where $\varepsilon = k_{ij}d_{ij}^2$ is the energy scale, and $s_{ij} = \delta_{ij}/d_{ij}$ is the dimensionless overlap. We assume that all the bonds have the same ε value, so the spring constant k_{ij} may vary (since d_{ij} is not constant). All results are reported in units of ε and d_B.

The packings were prepared via a quench from a random initial state at *fixed* area fraction $\phi = \frac{\pi}{4}L^{-2}\sum_{i=1}^{N} d_i^2$, where L is the size of the simulation box. For all results presented here, $L = 320d_A$. We study several different ϕ spaced linearly from 0.925 down to 0.85. The dimensionless ϕ is defined as the ratio between the particles' area and the total available area. We perform energy minimization with the LAMMPS software package [17] with the conjugate gradient method. The simulations were run until a force tolerance criterion was met. We used a criterion that no component of force on any particle exceed 10^{-7} times the average pressure at the given volume fraction. A custom code was developed to perform all linear response analysis (point load and homogeneous deformation) using the sparse linear solver routines in the SciPy toolkit. Quenching the large system took the majority of the CPU time and it was comparatively trivial to perform the linear response calculations once the relaxed mechanical equilibrium configurations had been obtained.

III. POINT RESPONSE

We start here by studying the linear response to a point force. *Macroscopically*, these systems have well defined average isotropic elastic modulus tensor, where it can be described by only two elastic moduli, the bulk modulus K and the shear modulus μ. The Fourier transform of the elastic Green's function of the system scales as q^{-2}. Since the system is disordered and heterogeneous; i) the response to a point load will not precisely follow the homogeneous continuum solution, and ii) each particular choice of location to apply the load will result in a different response function. However, on average, and at long lengths, we expect continuum homogeneous elastic-

ity to provide a good description. The question here is how the deviations from the continuum description die away at long lengths and how this depends on proximity to jamming.

A. Linear Response

Following standard procedures, we can expand the energy to second order in the displacements about an equilibrium configuration:

$$\Delta\mathcal{U} = \frac{1}{2}\sum_{ij} u_{i\alpha} H_{i\alpha j\beta} u_{j\beta} + \mathcal{O}(u^3) \tag{1}$$

where $u_{i\alpha}$ is the displacement of particle i and $H_{i\alpha j\beta} = \partial^2\mathcal{U}/\partial r_{i\alpha}\partial r_{j\beta}$ is the Hessian matrix. Here we denote the Cartesian components of vectors and tensors by Greek indices. The displacement in response to an external force must satisfy the linear response equation

$$\sum_j H_{i\alpha j\beta} u_{j\beta} = F^{\rm ext}_{i\alpha}. \tag{2}$$

We solve equation (2) numerically for the displacements $u_{i\alpha}$ using the sparse matrix routines in the SciPy library. In order to apply the point force, a particle is chosen at random, and its center defines the origin for interpolation and Fourier decomposition. In order to maintain mechanical stability, a compensation force of $F_y = F/N$ is applied on all particles so that $\sum_i F^{\rm ext}_{iy} = 0$ [18]. Here F is the magnitude of the external force and N is the total number of particles. A typical example for the field $u_{i\alpha}$ is shown in Fig. 1(a).

B. Continuum Solution

For a homogeneous, isotropic, linear elastic medium, the elastic properties of the system are fully described by the bulk modulus K and shear modulus μ. The point response, the Green's function for the linear elasticity operator, can be obtained simply in Fourier space (see appendix A), where one obtains

$$\begin{aligned} u^{\rm cont}_L(\mathbf{q}) &= \frac{F\,\sin(\theta)}{(K+\mu-p)q^2\ V}, \\ u^{\rm cont}_T(\mathbf{q}) &= \frac{F\,\cos(\theta)}{(\mu-p)q^2\ V}. \end{aligned} \tag{3}$$

Here, $u^{\rm cont}_L(\mathbf{q})$ and $u^{\rm cont}_T(\mathbf{q})$ are the longitudinal and transverse amplitudes of the displacements, F is the applied force magnitude, θ is the angle of the force vector with respect to the x axis, and V is the volume (area in two dimensions). Figure 1(b) illustrates a typical continuum solution in real space, obtained by taking an inverse Fourier transform of the above equation.

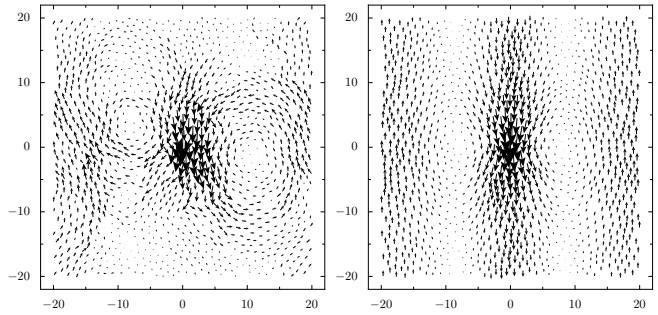

(a)Actual point response (b)Continuum estimate

FIG. 1: Arrows represent the displacements in response to a point force.

Several features in the continuum solution in Figure 1 are worth discussing. Note that the spatial structure of the continuum solution depends on the ratio of K to G (or, equivalently, the Poisson ratio). Although K/G differs by a factor of 10 the differences between the two continuum solutions is difficult to discern in real space. The differences become more obvious when we perform a Fourier decomposition below. Furthermore, we see that the systems closer to jamming are further from the continuum result. We quantify this departure in Fourier space below.

C. Displacement Field Decomposition

We present the actual point response by its Fourier longitudinal and transverse amplitudes, $u_L(\mathbf{q})$ and $u_T(\mathbf{q})$, where $\mathbf{q}$ is the wave vector. To obtain the data, we interpolate the discrete displacements $u_{i\alpha}$ on a regular *fine* grid of size $\sqrt{N_g} \times \sqrt{N_g}$ and then take the two-dimensional discrete Fourier transform of the interpolated field $u_\alpha(\mathbf{r}_j)$ to obtain the corresponding longitudinal and transverse components

$$\begin{aligned} u_L(\mathbf{q}) &= \sum_j u_\alpha(\mathbf{r}_j) n_\alpha\ e^{i\mathbf{q}.\mathbf{r}_j}, \\ u_T(\mathbf{q}) &= \sum_j u_\alpha(\mathbf{r}_j) n^\perp_\alpha\ e^{i\mathbf{q}.\mathbf{r}_j}. \end{aligned} \tag{4}$$

with $\mathbf{q} = 2\pi L^{-1}(n\hat{\mathbf{x}} + m\hat{\mathbf{y}})$ where m and n are integers and $\hat{\mathbf{x}}$ and $\hat{\mathbf{y}}$ are unit vectors along the x and y axes and $q^2 = \mathbf{q}.\mathbf{q}$. We take $\sqrt{N_g}/L = 3/d_A$ so that the mesh is just a bit finer than the particle spacing. Here $n_\alpha = q_\alpha/q$ is the unit vector along $\mathbf{q}$ and $n^\perp_\alpha$ denote the perpendicular direction. We then calculate the two-dimensional power spectra $s_L(\mathbf{q})$ and $s_T(\mathbf{q})$ on the two-dimensional q space averaged over position and members in the ensemble.

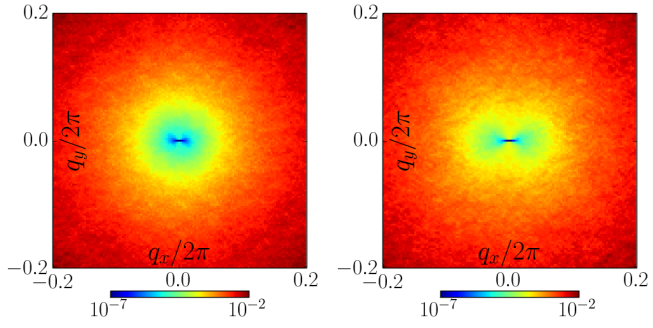

(a)$q^4 s_L(\mathbf{q})$ at $\phi = 0.85$ (b)$q^4 s_L(\mathbf{q})$ at $\phi = 0.925$

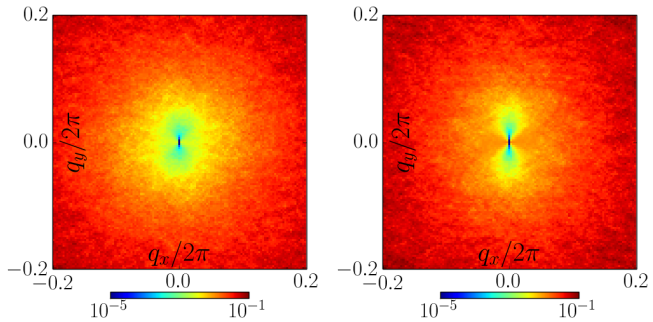

(c)$q^4 s_T(\mathbf{q})$ at $\phi = 0.85$ (d)$q^4 s_T(\mathbf{q})$ at $\phi = 0.925$

FIG. 2: Maps of $q^4 s_L(\mathbf{q})$ and $q^4 s_T(\mathbf{q})$ using a decimal log scale plotted for $\phi = 0.85$ and $\phi = 0.925$.

$$s_L(\mathbf{q}) = \frac{1}{N_g}\frac{|u_L(\mathbf{q})|^2}{\langle \mathbf{u}.\mathbf{u}\rangle},$$
$$s_T(\mathbf{q}) = \frac{1}{N_g}\frac{|u_T(\mathbf{q})|^2}{\langle \mathbf{u}.\mathbf{u}\rangle}, \quad (5)$$

where $\langle \mathbf{u}.\mathbf{u}\rangle = N_g^{-1}\sum_i \mathbf{u}(\mathbf{r}_i).\mathbf{u}(\mathbf{r}_i)$ is the mean squared displacements [27].

Figure 2 displays the ensemble averaged structure factors $s_L(\mathbf{q})$ and $s_T(\mathbf{q})$ (rescaled by q^{-4}) for $\phi = 0.85$ and $\phi = 0.925$. The structure factors $s_L(\mathbf{q})$ and $s_T(\mathbf{q})$ rescaled by q^{-4} measured along $\theta = 0$ and $\theta = \pi/2$ are shown in Figs. 3 and 4 for $\phi = 0.85$ (left) and $\phi = 0.925$ (right). The averages were calculated by binning according to log q along q_x and q_y on the two-dimensional q grid. The dashed lines in the plots represent the continuum predictions $q^4 s_L^{\rm cont}(\mathbf{q})$ and $q^4 s_T^{\rm cont}(\mathbf{q})$ which can be derived from Eq. (3)

There are several important observations to make about these plots. First, note that $u_L^{\rm cont}(\mathbf{q})$ is precisely zero at $\theta = 0$, as the applied force contains zero longitudinal power along that direction. This is also true for $u_T^{\rm cont}(\mathbf{q})$ at $\theta = \pi/2$. Surprisingly, non-zero longitudinal power along $\theta = 0$ and transverse power along $\theta = \pi/2$ are present (circles in Fig. 3 and squares in the Fig. 4) when they would be expected to be zero from the continuum solution. Above a wave vector of roughly

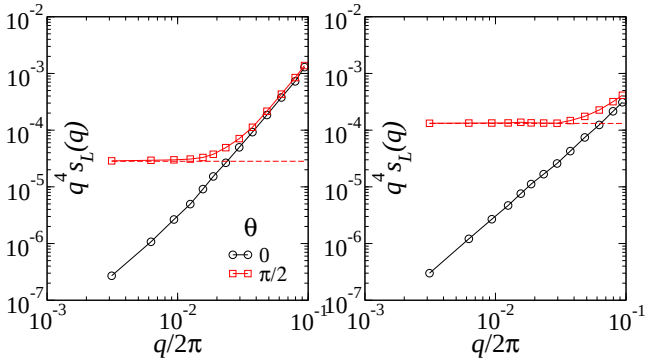

FIG. 3: $q^4 s_L(q)$ for cuts along the axis at $\theta = 0$ and $\theta = \pi/2$ at $\phi = 0.85$ (left) and $\phi = 0.925$ (right) compared with the continuum solution (dashed lines). Note that the continuum solution predicts precisely zero power for $\theta = 0$.

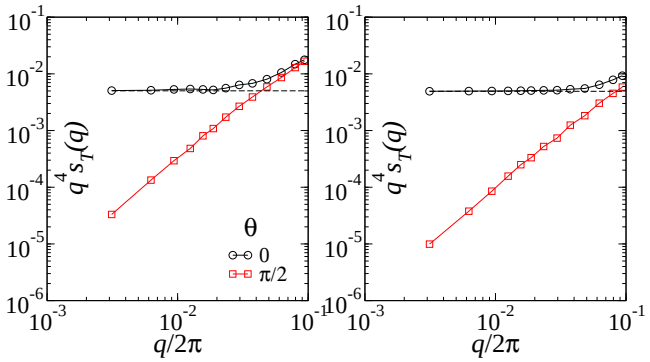

FIG. 4: $q^4 s_T(q)$ for cuts along the axis at $\theta = 0$ and $\theta = \pi/2$ at $\phi = 0.85$ (left) and $\phi = 0.925$ (right) compared with the continuum solution (dashed lines). Note that the continuum solution predicts precisely zero power for $\theta = \pi/2$.

$q/2\pi \approx 0.1$, corresponding to less than $\lambda \approx 10$, there is very little of the anisotropy expected from continuum mechanics, and the power essentially consists of high frequency, isotropic, noise.

Now let us compare $s_L(\mathbf{q})$ at $\theta = \pi/2$ and $s_T(\mathbf{q})$ at $\theta = 0$ to their continuum expressions. At low q (long wave length), the actual response compares well with the continuum solution (dashed curves) – with both showing q^{-4} behavior for small wave numbers. We emphasize that there are no free parameters in the fit to the continuum values (dashed); the global elastic moduli are measured independently using homogeneous linear response. For short wavelength, however, the continuum solution badly underestimates the power. The valid range of linear elasticity extends out to a larger q (smaller wave length) at $\phi = 0.925$ (right) than $\phi = 0.85$ (left) for both longitudinal and transverse structure factors. In other words, elasticity is only valid at very long wave length near jamming.

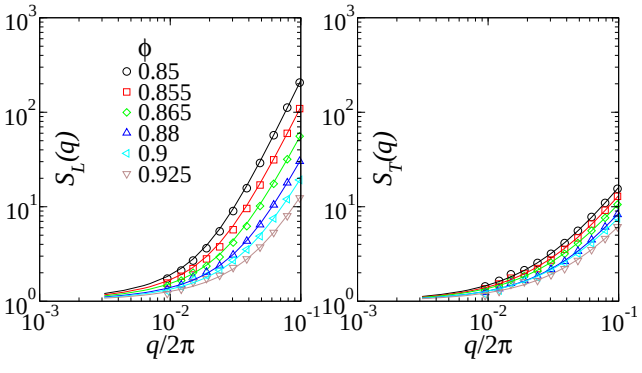

FIG. 5: $S_L(q)$ versus $q/2\pi$ (left) and $S_T(q)$ versus $q/2\pi$ (right) for different ϕ.

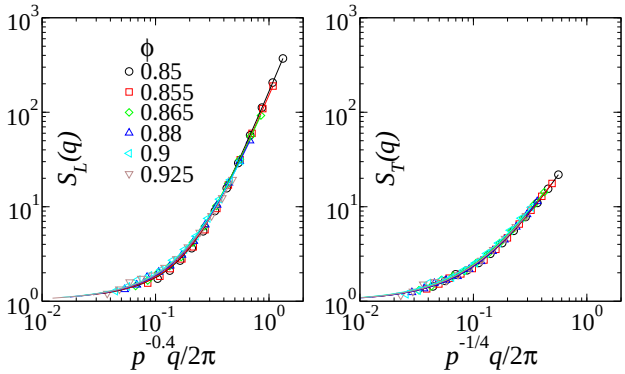

FIG. 6: $S_L(q)$ versus $p^{-0.4}q/2\pi$ (left) and $S_T(q)$ versus $p^{-0.25}q/2\pi$ (right) for different ϕ.

For simplicity, we compute the angle averaged structure factors $s_L(q)$ and $s_T(q)$ as the following: $\log s_L(q) = \langle \log s_L(\mathbf{q})\rangle_\theta$ and $\log s_T(q) = \langle \log s_T(\mathbf{q})\rangle_\theta$ where $\langle\rangle_\theta$ denotes averages over θ. We define the scaled structure factors as

$$S_L(q) = \frac{s_L(q)}{s_L^{\rm cont}(q)}, \qquad S_T(q) = \frac{s_T(q)}{s_T^{\rm cont}(q)}, \tag{6}$$

for $q \neq 0$. Here $s_L^{\rm cont}(q)$ and $s_T^{\rm cont}(q)$ are the isotropic continuum predictions We perform an isotropic averaging in the log, i.e. $\log\,|u_T^{\rm cont}(q)|^2 = \frac{1}{\pi}\int_0^\pi \log|u_T^{\rm cont}(q,\theta)|^2 d\theta$ which leads to $|u_T^{\rm cont}(q)|^2 = F^2/4\mu^2 q^4 V^2$. [28]

$S_L(q)$ and $S_T(q)$ measured for different ϕ and shown in Fig. 5. Qualitatively similar behavior is found for $S_L(q)$ and $S_T(q)$ at various packing fractions: they start at very high values for large q, go down as q decreases, and finally asymptote to unity as $q \to 0$ – which implies that elasticity works perfectly in that limit. This q-depence is more pronounced in the longitudinal power than it is in the transverse power, the slope of the $\log q^4 s$ vs. $\log q$ curve is much steeper at high q for the longitudinal case, and, at any ϕ and q, the longitudinal field has a stronger departure from the continuum solution. It is also clear that the longitudinal power is more sensitive to ϕ than the transverse power.

In Fig. 6, we show that the data can be made to collapse for various ϕ when plotting $S_L(q)$ versus $p^{-0.4}q/2\pi$ and $S_T(q)$ versus $p^{-0.25}q/2\pi$. That is, the characteristic length scales, denoted by ξ_L and ξ_T for the longitudinal and transverse modes, are $p^{-0.4}$ and $p^{-0.25}$ respectively. These scalings are consistent with divergence at jamming transition. The $p^{-0.25}$ is the same ξ_T measured by Lerner and co-workers [13], while the $p^{-0.4}$ scaling for ξ_L is closer to the measurements of Ellenrboek *et. al* [3] for the force fluctuations in a dilation test.

IV. LOCAL ELASTIC MODULI

The presence of disorder in an amorphous matter gives rise to strong fluctuations in the local elastic constants particularly at small scales. As discussed in Section III, linear isotropic homogeneous elasticity assumes that these heterogeneities are negligible. In fact, the severe non-continuum behavior observed in the point response – which is intensified near jamming – is due to the inherent spatial inhomogeneities in the structure [19]. Tsamados et al. [20] attempted to associate a characteristic scale to the elastic heterogeneities by measuring the local elastic properties at different coarse-graining sizes. On one hand, they found that the modulus converged rapidly to the continuum limit, but on the other hand, argued for a non-trivial length scale present in the structure of the displacement fields in response to homogeneous strain. A similar study was performed in reference [21] to measure spatial distributions of the local moduli in glasses. In that work, there was no emergent lengthscale detected. Neither of these works checked behavior near jamming.

We focus here on the scale dependence of the average shear modulus. We use a systematic coarse-graining approach and monitor the convergence of shear modulus value toward its bulk limit. The scale dependence of the local shear modulus is quantified by applying homogeneous shear strain using no slip boundary conditions with boxes of various size, R. This pinning at the boundary enhances the modulus by restricting the non-affine relaxations which are responsible for a reduction in the modulus in unconstrained systems. The response to an applied perturbing force in the form of a transverse wave is also used to study the probe-scale dependence of the modulus. In contrast to the no slip boundary driving, the modulus measured with the plane-wave perturbation converges quickly to the continuum limit and is essentially insensitive to ϕ.

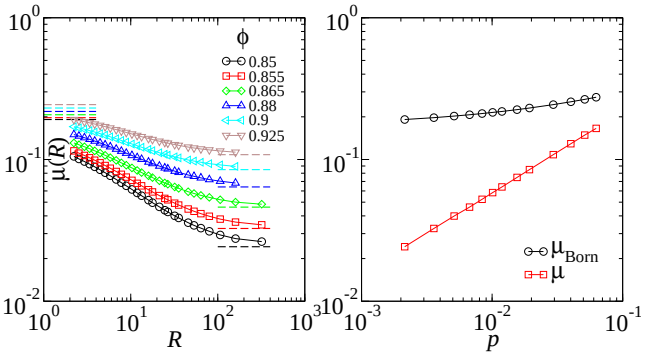

FIG. 7: Shear modulus $\mu(R)$ plotted against R at different ϕ (left) and $\mu_{\rm Born}$ and μ vs. p (right). The dashed lines indicate $\mu_{\rm Born}$ $(R \to 0) and \mu$ $(R \to \infty)$.

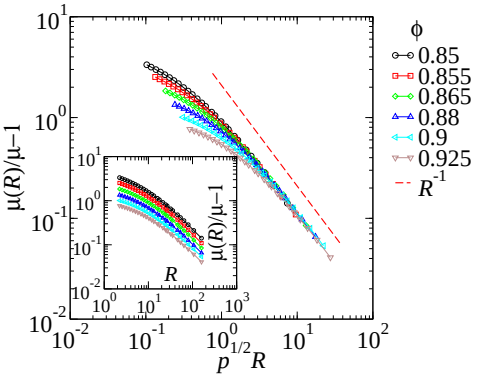

FIG. 8: $\mu(R)/\mu - 1$ plotted against $p^{0.5}R$ at different ϕ. In the inset, $\mu(R)/\mu - 1$ versus R is shown. The dashed line shows R^{-1}.

A. Constrained Homogeneous Shear

The local elasticity tensor relates the changes in the local stress tensor to an applied uniform strain in an elastic material. As usual [22], one may divide the modulus into a homogeneous, or Born, term and an inhomogeneous correction. The local Born shear modulus, $\mu_{\rm Born}(\mathbf{r}_i)$, is the derivative of the stress when the particles are forced to follow a perfectly homogeneous deformation field; the so-called Cauchy-Born rule. It may be computed by carrying out a summation over all pairs of interacting particles j with particle i [as in Eq. (B2)]. The bulk Born shear modulus $\mu_{\rm Born}$ – derived in Appendix B – is simply the spatial average of $\mu_{\rm Born}(\mathbf{r}_i)$, i.e. $\mu_{\rm Born} = \langle \mu_{\rm Born}(\mathbf{r}_i) \rangle$. In order to define the *net* local shear modulus locally in a sub-region $\Omega \in V$, the linear response equation [shown later in Eq. (9)] may be solved with all exterior particles held *fixed*, i.e. $\delta u_{i\alpha} = 0$, and the local moduli then can be defined. The crucial feature of the protocol is that while the interior particles can move nonaffinely, the exterior particles act as a fixed, rigid boundaries.

Figure 7 right illustrates the pressure dependence of $\mu_{\rm Born}$ and μ for the full system under the usual periodic boundary conditions. Near jamming, μ decreases toward zero as expected, as the contribution of the correction term $\mu_c = \mu_c(R \to \infty)$ grows relative to the Born term $\mu_{\rm Born}$. The Born term shows little sensitivity to p and converges to a well defined value as already shown in the seminal work by O'Hern *et. al.* [1].

We divide the simulation cell into squares of varying length R and follow the above procedure for each box to find a coarse-grained shear modulus $\mu(\mathbf{r}_i, R)$. The local *correction* to the shear modulus is defined as $\mu_c(\mathbf{r}_i, R) = \mu_{\rm Born}(\mathbf{r}_i) - \mu(\mathbf{r}_i, R)$ and its spatial average is $\mu_c(R) = \langle \mu_c(\mathbf{r}_i, R) \rangle$. We plot $\mu(R)$ – which is a spatial average $\mu(R) = \langle \mu(\mathbf{r}_i, R) \rangle$ – against R in Fig. 7 left. It exhibits significant size dependence. At the short length-scales, very little inhomogeneous correction is allowed because the particles are constrained to move approximately affinely. Then $\mu_c \approx 0$ or $\mu \approx \mu_{\rm Born}$. At longer length-scales, $\mu(R)$ decreases monotonically toward the continuum value computed for periodic systems, $\mu = \mu(R \to \infty)$. At larger R, increasingly longer wavelength inhomogeneous corrections are allowed to $\mu(R)$, while the contribution of the bulk particles increases compared to the Born term $\mu_{\rm Born}$ which is scale independent.

From the assumption that particles move only affinely on the perimeter of the box, one can estimate that $\mu_c(R) \propto N_{\rm Bulk}/N_R$ where N_R is the total number of particles in a square of length R and $N_{\rm Bulk}$ is the number of particles in the bulk. The number of particles on the perimeter, which we denote by $N_{\rm Perim}$, is proportional to R. Now $N_{\rm Bulk} = N_R - N_{\rm Perim}$ and we have that $N \propto R^2$. Hence $\mu_c(R) = \mu_c(1 - \xi/R)$ where ξ has dimension of length and determines how quickly $\mu_c(R)$ should reach its asymptote μ_c. Upon using this relation, we obtain the following formula for $\mu(R)$ with an explicit dependence on R (and of course p)

$$\mu(R) = \mu + \mu_c \frac{\xi}{R}. \tag{7}$$

Now, $\xi\mu_c/\mu$ is a characteristic length which is the R above which one almost recovers the true global modulus; namely $\mu(R \gg \frac{\mu_c}{\mu}\xi) \approx \mu$. Evidently(see Fig. 7 left) this characteristic length depends on p. In Fig. 8, we show that the data can be made to collapse, at large R, for various ϕ when plotting $\mu(R)/\mu - 1$ versus $p^{\frac{1}{2}}R$. The simple scaling theory captures R^{-1} asymptotic approach of $\mu(R)$ to μ (Fig. 8 inset). Physically speaking, the sample size R needed to converge to the fully relaxed shear modulus diverges as $p^{-1/2}$ which is close to the l_* result [6, 7]. For example, if one wants to obtain a measurement of the modulus that has converged to within 10% of the infinite size limit, one needs to use a box which is larger than $p^{0.5}R \approx 10$.

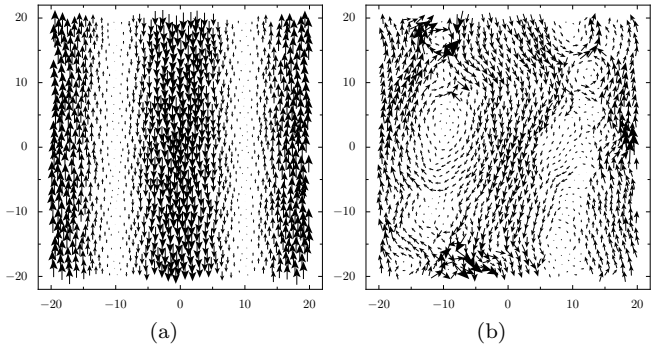

FIG. 9: (a) The applied forces $F_{i\alpha}^{\rm ext}$ and (b) the corresponding response $u_{i\alpha}$ for a typical small system.

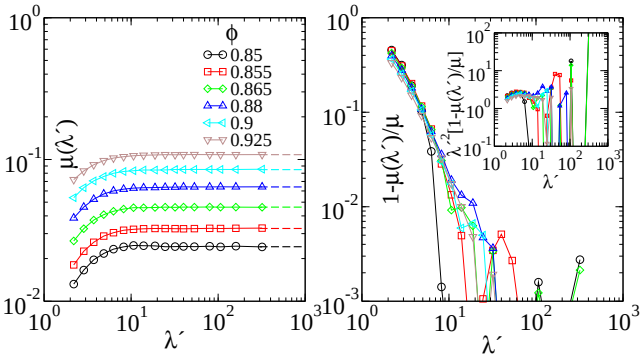

FIG. 10: Dependence of the shear modulus $\mu(\lambda')$ (left) and the relative error on the shear modulus $1-\mu(\lambda')/\mu$ (right) on the wavelength $\lambda'=2\pi/q'$ for various ϕ. The inset is the same as the main plot but rescaled by λ'^2. The dashed lines represent μ.

B. Elastic Wave Response

Response to plane wave forcing with a varying wavelength is also used to quantify the scale dependence in the shear modulus. We perturb the system with an external force vector $F_{i\alpha}^{\rm ext}=F\psi_{i\alpha}$ in the form of an ordinary unit transverse plane wave where $\psi_{j\alpha}=n_\alpha e^{i\mathbf{q}'\cdot\mathbf{r}_j}/\sqrt{N}$. Here $\mathbf{q}'$ is the wave vector and n_α is the unit polarization vector perpendicular to $\mathbf{q}'$. We solve $\sum_j H_{i\alpha j\beta}u_{j\beta}=F\psi_{i\alpha}$ to find the response, $u_{i\alpha}$. Typical snapshots of the imposed force field $F_{i\alpha}^{\rm ext}$ and resulting displacements $u_{i\alpha}$ are depicted in Fig. 9 for a typical small system. It is evident that the response contains deviations from the simple plane wave solution which is expected for a homogeneous medium. We turn now to the calculation of the elastic coefficient μ using the elastic wave response. The change in energy of the final state is given by $\Delta\mathcal{U}(q')=\frac{1}{2}u_{i\alpha}H_{i\alpha j\beta}u_{j\beta}$. We find that (see appendices)

$$\mu(q')=p+F^2[\Delta\mathcal{U}(q')\ q'^2V/N]^{-1}. \tag{8}$$

Our results for the shear modulus $\mu(\lambda')$ as a function of the wavelength, $\lambda'=2\pi/q'$, of the applied force are collected in Fig. 10 left. It looks like there is very little λ' dependence. $\mu(\lambda')$ reaches the continuum value at rather small λ'. This crossover point is *insensitive* to ϕ. In Fig. 10 right, the quantity $1-\mu(\lambda')/\mu$ is shown to decay as λ'^{-2} at small λ', with a pre-factor that is independent of ϕ (see the rescaled data by λ'^{-2} in the inset). In effect, all these curves can be rescaled simply by the continuum value of μ. The λ' dependence at small λ' is simply what would be seen for a phonon dispersion as it approaches the Brillouin zone boundary. To see this, suppose that the eigenmodes of the Hessian can be approximated as plane waves and that the associated eigenvalues scale as $\sin^2 q$. One then obtains $\Delta\mathcal{U}\propto 1/\sin^2 q$. So then we have $\mu\propto\sin^2 q/q^2$. Fig. 10 right shows that this simple scenario for approach to the continuum limit holds.

We conclude that the wave method gives a measure for the modulus which is surprisingly *in*sensitive to ϕ and converges to the continuum result very quickly. The weak λ' dependence is simply due to the dispersion effect which manifest itself at small λ' values. However, in the constrained box method these corrections exhibit a strong scale dependence, as particles are pinned on the boundary while the wave method does not constrain any particle motion. Thus the pinning at the boundaries seems absolutely crucial to bring out the rigidity length, l_*, governing the jamming transition.

V. UNCONSTRAINED HOMOGENEOUS DEFORMATION

The inhomogeneous local response of amorphous packings subject to a homogeneous global deformation is a direct consequence of the underlying structural disorder. In the Fourier decomposition of their nonaffine displacement field, Leonforte et al. [16, 23] observed that the longitudinal and transverse powers were proportional to q^{-2} with a slight excess at long wavelengths.

One important question is to what extent the observed behavior in Green's function, discussed in previous section, carries over to homogeneous applied strain. In this section, we investigate the nonaffine displacement field using an *unconstrained* homogeneous strain applied to a periodic cell. We focus on two modes of global deformation: isotropic dilation (compression) and pure shear. [29]

A. Nonaffine Response

Macroscopic deformations of the sample are performed by changing the shape of the periodic box via the deformation gradient tensor $F_{\alpha\beta}$. Changes in $F_{\alpha\beta}$ correspond to affine transformations of all the particles following the cell shape. At zero temperature, an infinitesimal defor-

mation of the system is often performed in two steps. First, starting from a local minimum, the particle coordinates affinity follow the change of the cell coordinate. The real space position of particle i is thus mapped from $r_{i\alpha}$ to $F_{\alpha\beta}r_{i\beta}$. Second the particles are allowed to relax to the nearest equilibrium position $r_{i\alpha}$, with $F_{\alpha\beta}$ being fixed. The nonaffine part of the deformation is then characterized by $\delta u_{i\alpha} = u_{i\alpha} - u_{i\alpha}^{\rm aff}$ where $u_{i\alpha}^{\rm aff} = (F_{\alpha\beta} - \delta_{\alpha\beta})r_{i\beta}$.

For now, let us move on to how we may derive these nonaffine fields in response to some prescribed mode of deformation parametrized by $F_{\alpha\beta}$. The equation of motion for $\delta u_{i\alpha}$ is obtained by solving [22]

$$\sum_j H_{i\alpha j\beta} \frac{\delta u_{j\beta}}{\eta_{\sigma\gamma}} = \Xi_{i\alpha}^{\sigma\gamma}, \tag{9}$$

where $\eta_{\alpha\beta} = (F_{\gamma\alpha}F_{\gamma\beta} - \delta_{\alpha\beta})/2$ is the Lagrangian strain tensor and $\Xi_{i\alpha}^{\beta\gamma} = -\partial^2\mathcal{U}/\partial r_{i\alpha}\partial\eta_{\beta\gamma}|_{\eta_{\beta\gamma}\to 0}$ is the field of forces which results from an affine deformation of all the particles. The above equation shows that $\delta u_{i\alpha}$ is just the linear response to these extra forces under deformation along $\eta_{\alpha\beta}$.

For a given relaxed configuration we first compute $\Xi_{i\alpha}^{\sigma\gamma}$ and then solve for $\delta u_{i\alpha}$ numerically.For small systems, we have checked that this procedure gives agreement with the less precise procedure of applying a small finite deformation and performing a subsequent energy minimization in LAMMPS.

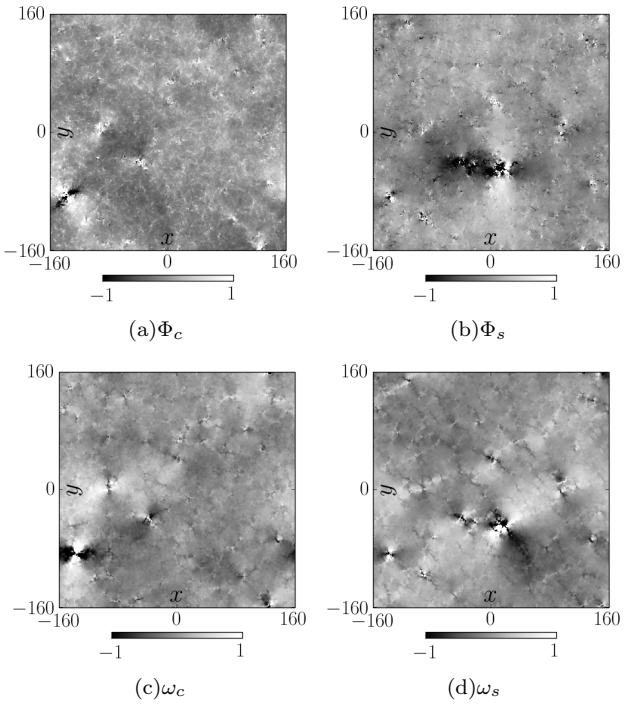

FIG. 11: Real space images of dilatancy, Φ, (top: a and b) and vorticity, ω, (bottom: c and d) generated for imposed compression (left: a and c) and shear (right: b and d) at $\phi = 0.925$.

B. Nonaffine Displacements Decomposition

To analyze the displacements in real space, we focus on the dilatancy, $\Phi = \nabla \cdot \vec{u}$, and vorticity, $\omega = \partial_x u_y - \partial_y u_x$, where $\vec{u}$ is the non-affine displacement and the derivatives are calculated by finite difference on our mesh. Figure 11 shows Φ_c and ω_c resulting from a globally applied compression (denoted by the subscript 'c' for compression) at left and Φ_s and ω_s resulting from a globally applied area-preserving shear (denoted by the subscript 's' for shear) at right for a single realization at $\phi = 0.925$. The applied shear is axial in sense $\epsilon_{xx} > 0$, $\epsilon_{yy} = -\epsilon_{xx} < 0$, $\epsilon_{xy} = \epsilon_{yx} = 0$. Note that we are in the linear response regime, so, apart from an overall sign in the displacement and strain field, there is no distinction between imposing compression and dilation or between imposing two different area-preserving shear strains with opposite sign. The images are exceedingly rich with organization on several scales.

For the case of applied compression, one observes at least two different kinds of regions: compression zones where compact clusters have higher than average compaction, and shear zones where local shears are activated. The compression zones and shear zones manifest themselves differently in Φ_c and ω_c. The most obvious feature in the Φ_c and ω_c plots is the strong shear zone at $x \approx -140, y \approx -100$. The quadrupolar signature in ω and ϕ oriented at an angle of $\pi/4$ relative to each other are the hallmark of an Eshelby shear transformation [24]. This particular shear zone has been excited in an orientation which is in extension along, roughly, $\pi/4, 5\pi/4$, and, correspondingly, in contraction 90 degrees away along $3\pi/4, 7\pi/4$. When observing many systems of size $L = 320$, we typically observe one to several of these strong shear zones under compression for any given sample. Any configuration may have a large shear with a particular orientation, but, on average, orientations are distributed in an unbiased way since the applied isotropic loading cannot select any preferred orientation. As we will see below, this results in an isotropic power spectrum for both Φ_c and ω_c. The compaction zones are far less visually pronounced than the shear zones. They do not stand out as far from the background noise level. They are partially visible in the vorticity, but their contribution to the vorticity is far less dramatic than the shear zones. In the dilatancy, Φ, they show up as small, white compact clusters of compaction. They have some shear associated with them, but they are primarily dilatational in nature.

For the case of applied shear, the local response is, not surprisingly, dominated by shearing motion. The organization is most easily seen in the vorticity field, ω_s. There are many local shear zones with quadrupolar symmetry of the type observed in compression, but now, owing to the global anisotropy induced by the shear, they are all aligned primarily in the correct sense, with positive vor-

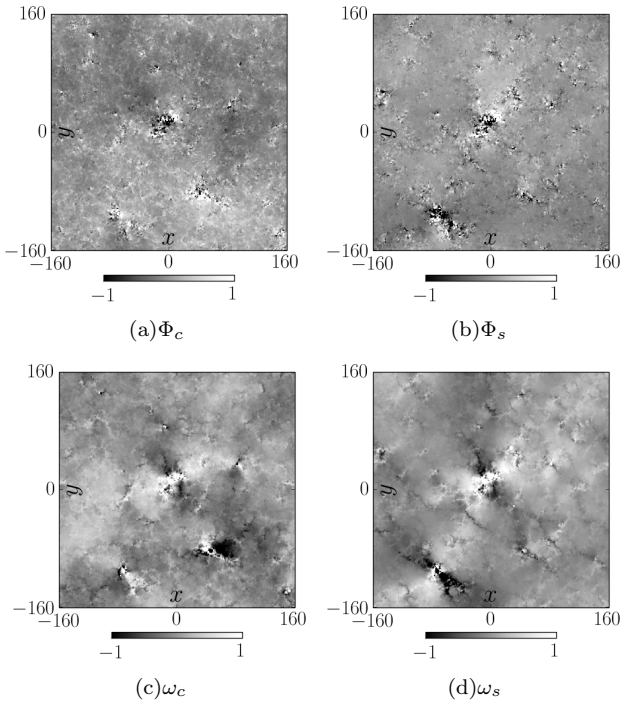

FIG. 12: Real space images of dilatancy, Φ, (top: a and b) and vorticity, ω, (bottom: c and d) generated for imposed compression (left: a and c) and shear (right: b and d) at $\phi = 0.85$.

ticity along the $\pi/4, 5\pi/4$ orientation and negative vorticity along the $3\pi/4, 7\pi/4$ orientation as one would expect from a canonical Eshelby shear transformation. However, in addition to these isolated, strong, Eshelby fields, there is another kind of organization. There are weak lines in the background, reminiscent of the weak planes invoked to explain the anomalous viscoelastic response of emulsions [25]. The weak lines are long and tenuous and aligned with the shear in the same sense as the Eshelby zones: white lines along $\pi/4, 5\pi/4$ and black lines along $3\pi/4, 7\pi/4$. Whereas the cores of the Eshelby zones have strains that largely exceed the applied strain ($|\omega| > 1$), these weak lines in the background have strains that are a few tens of a percent of the applied strain ($|\omega| \approx 0.1-0.3$).

In figure 12 we plot the same Φ and ω fields in real space as in figure 11, but now for $\phi = 0.850$, nearest to the jamming transition. The result is surprising. On one hand, the ω field seems remarkably unchanged. Under shear, one still observes intense Eshelby fields outside the core of strong shear zones aligned in the appropriate sense. Under compression one can still make out individual Eshelby zones, with orientations that average out to something isotropic. On the other hand, the Φ fields look very different from the $\phi = 0.925$ case which was much further from the jamming transition. In shear, the centers of the Eshelby shear zones which appear as coherent with long ranged structure in the ω_s field and appear as noisy cores with very short wavelength oscillations in the Φ_s field where the material alternates strongly between dilation and compaction at very short wavelength. We suspect that the lack of coherent spatial structures in Φ_s is due to the incompressibility of the packings near jamming. The pressure at $\phi = 0.85$ is almost of factor of 100 times smaller than the pressure at $\phi = 0.925$, and the shear modulus is, correspondingly, almost a factor of 10 smaller with very little difference in the compression modulus. Therefore, one would expect very little dilatancy at all beyond wavelengths where continuum elasticity holds. This suppression of dilatancy at long wavelength is, in fact, precisely what we will show below when we discuss the power spectra.

Next we discuss the longitudinal and transverse structure factors, $s_L(\mathbf{q})$ and $s_T(\mathbf{q})$ in response to dilation $\eta_{\alpha\beta} = \epsilon\delta_{\alpha\beta}$ and pure shear $\eta_{\alpha\beta} = \epsilon(\delta_{\alpha x}\delta_{\beta x} - \delta_{\alpha y}\delta_{\beta y})$. The nonaffine displacements, computed from Eq. (9). As for the point-response above, the displacement fields are interpolated onto a fine grid and a discrete Fourier transform is subsequently performed to obtain $u_L(\vec{q})$ and $u_T(\vec{q})$. For differentiable vector fields in 2D, the Stokes-Helmholtz decomposition allows us to represent all the information in terms of the two scalar fields, Φ and ω, introduced above. These two are intimately related to the longitudinal and transverse decomposition of the displacement field. $\Phi(\mathbf{r})$ and $\omega(\mathbf{r})$ can be obtained from s_L and s_T by taking an inverse discrete Fourier transform of $u_L(\mathbf{q})$ and $u_T(\mathbf{q})$

$$\begin{aligned} \Phi(\mathbf{r}_j) &= \frac{1}{N_g}\sum_{\mathbf{q}} q u_L(\mathbf{q}) e^{i\mathbf{q}\cdot\mathbf{r}_j}, \\ \omega(\mathbf{r}_j) &= \frac{1}{N_g}\sum_{\mathbf{q}} q u_T(\mathbf{q}) e^{i\mathbf{q}\cdot\mathbf{r}_j}. \end{aligned} \tag{10}$$

where N_g is the number of grid points in our interpolation mesh. Alternatively, finite difference expressions for ϕ and ω in real space give almost identical values to these Fourier expressions at long wavelength and only small quantitative differences at short wavelength which do not affect any of the scaling behaviors observed in the power spectra shown below. The images presented above, in figures 11 and 12 were simply obtained by finite difference in real space, but images generated from the fourier representation look similar.

The nonaffine elastic response can be expected to arise from an isotropic homogeneous linear elastic medium perturbed by local contact forces with varying magnitudes and orientations [13, 15]. One expects the power spectrum, $s(q)$, of the displacement field to scale like $s \sim 1/q^2$ [15, 16, 23], so it is natural to rescale the power by q^{-2}. Note that this scaling behavior is consistent with two complementary interpretations. On one hand, a displacement field with power scaling like q^{-2} implies a strain field with power scaling like q^0. Gaussian random whitenoise is consistent with this scaling. On the other hand, the Eshelby solution itself has a far field form for the strain field that is also independent of the magnitude of q [24]. So one might alternatively interpret the

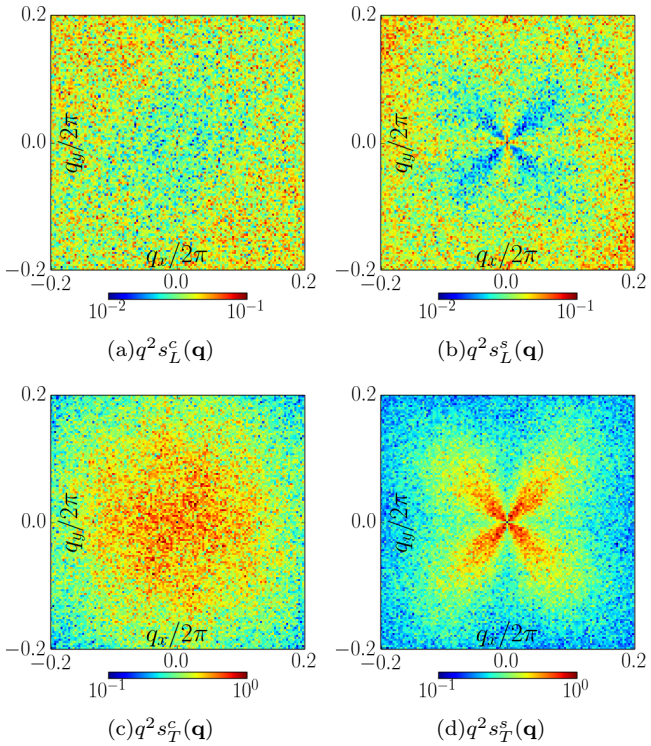

FIG. 13: Maps of the longitudinal (top) and transverse (bottom) scaled power spectrum, $q^2 s$ in dilation (left) and shear (right) plotted for $\phi = 0.925$ using a decimal log scale.

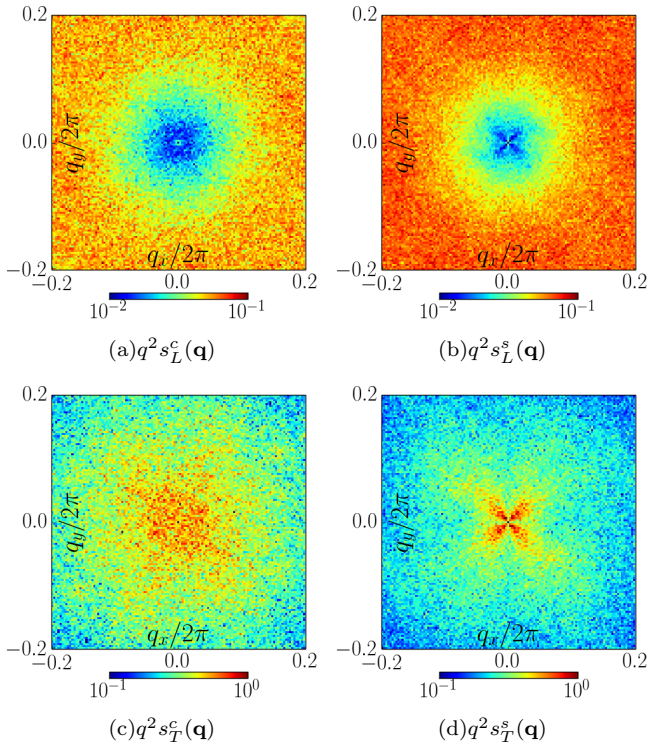

FIG. 14: Maps of the longitudinal (top) and transverse (bottom) scaled power spectrum, $q^2 s$ in dilation (left) and shear (right) plotted for $\phi = 0.85$ using a decimal log scale.

displacement and strain fields as arising from spatially uncorrelated Eshelby transformations. It is difficult to distinguish between these two interpretations based on an analysis of the power spectrum (or equivalently, two-point correlations in real space) alone.

In Fig. 13, we plot the ensemble averaged structure factors rescaled by q^{-2} at $\phi = 0.925$. We display $q^2 s_L^c(\mathbf{q})$ (top) and $q^2 s_T^c(\mathbf{q})$ (bottom) computed in dilation (left) and $q^2 s_L^s(\mathbf{q})$ and $q^2 s_T^s(\mathbf{q})$ in shear (right). The first observation is that the dominant behavior of all four quantities, $s_L^s, s_L^c, s_T^s, s_T^c$, is $s \sim q^{-2}$. This can be seen by virtue of the fact that, at low q, the color is essentially constant along any ray. This is in agreement with expectations based on the random contact force argument [15], or, alternatively on uncorrelated Eshelby transformations. The response to dilation (s_L^c, s_T^c) must be isotropic on average, but the response to shear (s_L^s, s_T^s) may be anisotropic. We see that *both* $s_T^s(\mathbf{q})$ *and* $s_L^s(\mathbf{q})$ show anisotropy. The character of the shear-induced anisotropy is opposite for the longitudinal and transverse response. For the transverse, the maximum power is along the lines of maximum shear ($\theta = \pm\pi/4$), while for the longitudinal, the maximum power is $\pi/4$ away from that. Transverse modes are enhanced along the directions of maximum shear, while longitudinal modes are suppressed along the directions of maximum shear. Anisotropy would be the naive expectation for the transverse power as it encodes information about local shearing motion. One might have been surprised to have seen the anisotropy in Φ, however, it can be seen as a natural consequence of the dilatancy field arising from the Eshelby fields. The Eshelby solution for shear transformation in a material with finite compression modulus contains shear along the directions of maximum shear and dilatancy at an orientation of $\pi/4$ away from the shear.

In figure 14, we plot the scaled power spectra for the system close to jamming at $\phi = 0.85$. Compared to the $\phi = 0.925$ case, there are several differences to note. First, the longitudinal power develops a characteristic length at $q/2\pi \approx 0.1$ in both compression ($q^2 s_L^c$) and shear ($q^2 s_L^s$). Above $q/2\pi \approx 0.1$, the spectrum is roughly flat, but below $q/2\pi \approx 0.1$, the scaled power decreases. In comparison, for the $\phi = 0.925$ case, $q^2 s_L^c$ and $q^2 s_L^s$ were both roughly flat throughout the range of q measured. At $q/2\pi \approx 0.1$, the longitudinal power has lost almost all of its anisotropy, while the transverse power retains it. Secondly, in shear, both longitudinal and transverse power are anisotropic, as was the case for $\phi = 0.925$. The transverse shear is largely unchanged, while the longitudinal shear is significantly suppressed at low q relative to $\phi = 0.925$.

In figure 15 and 16, we plot the scaled power along the special directions, $\theta = 0$ and $\theta = \pi/4$ for the case

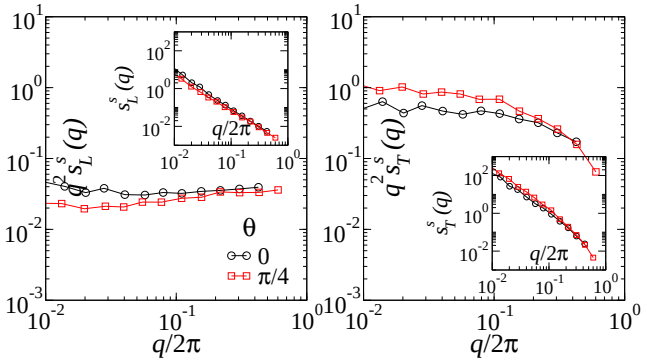

(a)

FIG. 15: $q^2 s_L^s(q)$ (left) and $q^2 s_T^s(q)$ (right) for cuts along the axis at $\theta = 0$ and $\theta = \pi/4$ at $\phi = 0.925$. The insets plot $s_L^s(q)$ and $s_T^s(q)$.

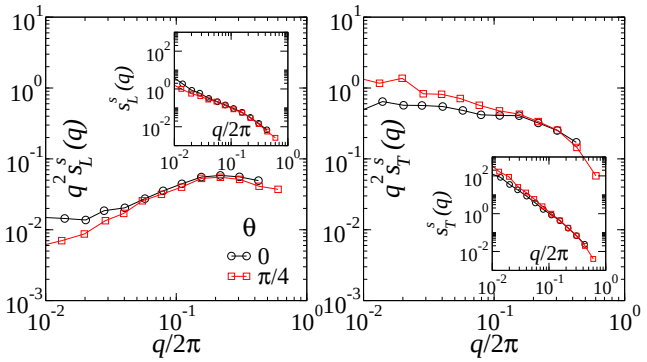

FIG. 16: $q^2 s_L^s(q)$ (left) and $q^2 s_T^s(q)$ (right) for cuts along the axis at $\theta = 0$ and $\theta = \pi/4$ at $\phi = 0.85$. The insets plot $s_L^s(q)$ and $s_T^s(q)$.

of applied shear. The trends we observed in the full 2D spectra become clearer here in the curves specialized to the two special orientations $\theta = 0$, and $\theta = \pi/4$. In all cases, the applied shear induces roughly the same amount of anisotropy in the power as the applied dilation. At long wavelength, there is roughly a factor of 2 more power along the direction of maximum resolved shear stress ($\theta = \pm\pi/4$) than there is along the other axis ($\theta = 0, \pi/2$). For the longitudinal response, the anisotropy is reversed, with more power along $\theta = 0$ than $\theta = \pi/4$ as observed in the full 2D spectra. The system near jamming has an enhancement of longitudinal power at large q and a suppression of power at small q. *The transverse power is remarkably insensitive to* ϕ, as one might have guessed from the real space images of ω or the full 2D power spectrum. Finally, as we pointed out for the 2D spectra, the Longitudinal response becomes *isotropic* at a much smaller q for $\phi = 0.85$ compared to $\phi = 0.925$. One would need to go out to very large wavelengths to observe the anisotropy. However, at those long wavelengths where s_L *is* anisotropic, the *magnitude* of the anisotropy ($s|_{\theta=0} \approx 2s|_{\theta=\pi/2}$) is roughly independent of ϕ.

As the response to compression is isotropic, we can take an isotropic average to improve the statistics and make comparisons at different volume fraction. We average the log of the power over angles: $\log[s_L^c(q)] = \langle \log[s_L^c(\mathbf{q})] \rangle_\theta$ and $\log[s_T^c(q)] = \langle \log[s_T^c(\mathbf{q})] \rangle_\theta$ where $\langle \rangle_\theta$ denotes averages over θ. These quantities are plotted in Fig. 17 for various ϕ. We make several important points here. First, $s_L^c(q)$ shown in Fig. 17(a) is much more sensitive to jamming than $s_T^c(q)$ does in Fig. 17(b), which is consistent with the Green's function behavior discussed in Section III. Secondly, the low-q values of $s_T^c(q)$ almost decay as q^{-2} [the plateau of $q^2 s_T^c(q)$ in Fig. 17(b)], while the tail of $q^2 s_T^c(q)$ for high-q values indicates a faster decay than q^{-2}. Far away from the jamming transition, $s_L^c(q)$ almost follows q^{-2} scaling. That is, the brown downward triangles in Fig. 17(a) are almost perfectly flat. As we approach jamming, however, we observe large deviations from the q^{-2} scaling at intermediate q where the decay gets very slow, which is in agreement with non-continuum behavior observed in Section III. Near jamming, one might recover the q^{-2} scaling for s_L at very large lengths, and our data is not inconsistent with this picture.

Fig. 18 shows the same quantities as Fig. 17, but for applied shear rather than compression. Strikingly, the spectra are almost identical. So we conclude that proximity to jamming has a pronounced effect on the longitudinal spectra but almost no effect on the transverse spectra regardless of whether shear or dilation is applied.

We summarize this section by concluding that the basic form for the displacement fields in response to either applied compression (or equivalently dilation) or shear is $s \sim q^2$. This q^{-2} scaling might be thought to arise either as a result of uncorrelated Eshelby transformation fields or as a result random contact forces perturbing an elastic medium. However, there are important departures from the q^{-2} behavior.While the longitudinal sector is sensitive to ϕ, the transverse sector is shockingly insensitive, both in applied compression and shear. The longitudinal response shows suppressed power at long wavelength as $\phi \to \phi_c$. In compression the power was isotropic as it must be. In shear, along the diagonal of the cell (maximum shear) we observed enhanced transverse (vorticity) power and suppressed longitudinal (dilatancy). This enhancement can be understood to arise from the alignment of the Eshelby fields with the applied shear. Near jamming, the anisotropy in the longitudinal sector can only be observed at the longest wavelengths where the power regains the q^{-2} scaling, but the magnitude of the anisotropy at those wavelengths is roughly a factor of 2 and is essentially independent of q and ϕ.

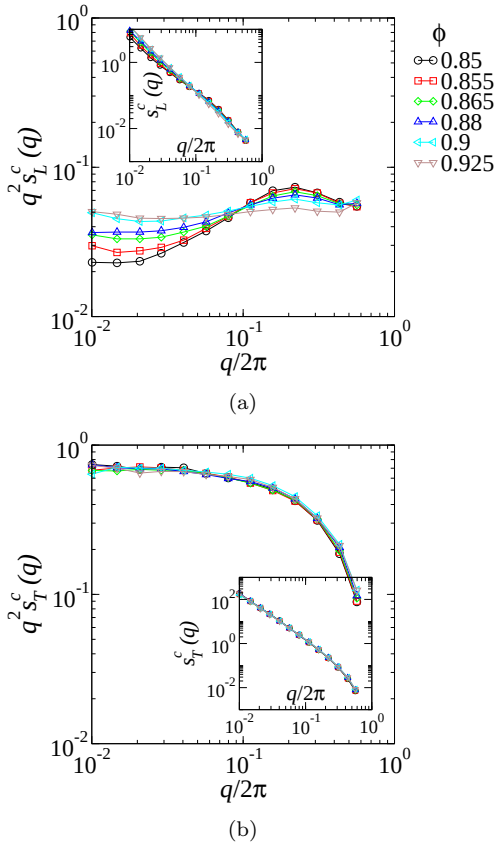

FIG. 17: $q^2 s_L^c(q)$ versus $q/2\pi$ (a) and $q^2 s_T^c(q)$ versus $q/2\pi$ (b) for different ϕ in *dilation*. In the insets, $s_L^c(q)$ and $s_T^c(q)$ are plotted against $q/2\pi$.

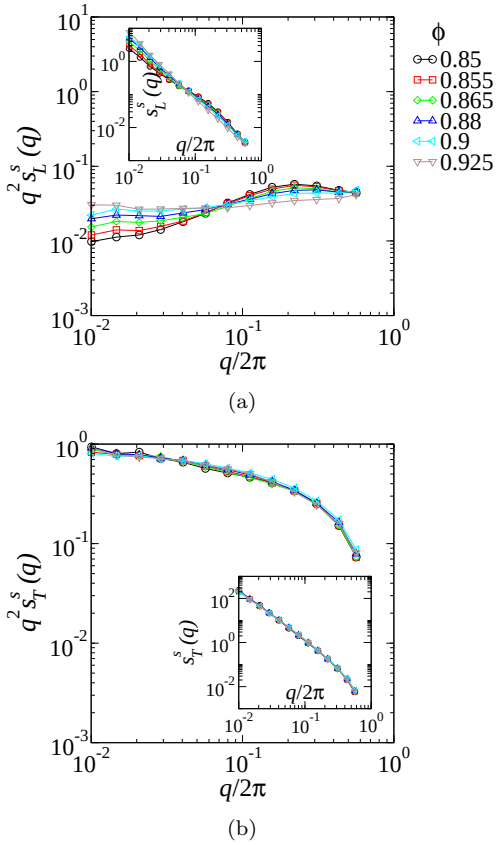

FIG. 18: $q^2 s_L^s(q)$ versus $q/2\pi$ (a) and $q^2 s_T^s(q)$ versus $q/2\pi$ (b) for different ϕ in *shear*. In the insets, $s_L^s(q)$ and $s_T^s(q)$ are plotted against $q/2\pi$.

VI. DISCUSSION AND SUMMARY

In this letter, we studied numerically the linear elastic mechanical response of disc packings above, but near, jamming. The packings were subjected to both homogeneous strain and point forcing. We also discussed the response of small subsystems to homogeneous strain subject to rigid, no slip boundaries. In the case of the point-like external force, the response displays a striking deviation from continuum behavior; at small wavelengths the response shows a clear departure from the expectations the extent of which increases near jamming. The observed behavior identifies a crossover length whose location depends on the proximity to jamming. In particular, the longitudinal response is governed by a length, ξ_L which diverges at jamming in a way similar to the rigidity length $l_* \sim p^{-0.5}$ invoked to explain the anomalies in the density of states, while the transverse response, ξ_T is governed by a length which diverges like $\xi_T \sim p^{-0.25}$.

Recently Lerner *et. al.* [13] have studied the response to an applied force dipole at contact. They showed that the response was governed by a length, $l_c \sim p^{-0.25}$, in apparent contradiction with the Ellenbroek *et. al.* [3], and argued that this length was related to an effective medium theory for the elasticity of the packing [14]. In this work, we showed that the point response contains two distinct lengths governing longitudinal and transverse sectors scaling differently with p. Ellenbroek's particle-inflation probe induces a radial displacement field with azimuthal symmetry. It is curl-free and should not be influenced by the transverse length scale. Lerner's dipole contains both longitudinal and transverse components, however, as we pointed out above, the ratio of the magnitudes of the transverse to longitudinal contributions goes like $(K+\mu)/\mu$ which diverges at jamming. So if one does not carefully isolate the longitudinal contribution, it will be swamped by the transverse contribution. This calls for an attempt to adapt the effective medium approach of During *et. al.* [14] to account separately for the longitudinal and transverse sectors.

For constrained homogeneous shear, we also identify a characteristic length associated with the size dependent average shear modulus. This length determines how quickly one recovers the underlying global shear constant for an unconstrained sample. We have shown that this length grows in precisely the same way as the rigidity lengthscale: $\xi \sim p^{-0.5}$. Our results indicate that, in all cases, although the transverse component of the response

makes the dominant contribution, the longitudinal component shows much more sensitivity to the jamming transition and much stronger dependence on q.

For the response to unconstrained homogeneous strain, in all cases, the basic form of the response is that the displacements scale like the wave vector: $|u(q)|^2 \sim q^2$. However, we find dramatically different departure from this behavior for the longitudinal (dilatancy) and transverse (vorticity) response. The longitudinal response to either compression/dilation or shear has a pronounced ϕ dependence – not inconsistent with the $\xi \sim p^{-0.5}$ rigidity scaling. The transverse sector is remarkably independent of ϕ. It is quite surprising that the transverse sector shows such very little ϕ dependence, and it is also quite surprising that the spectra seem so insensitive to the applied loading conditions: imposed dilation or shear.

We have presented three distinct probes based on linear elastic response to look for emergent characteristic lengths near jamming. One may ask how these three should be related. In spring networks, During *et. al.* [14] have suggested that two lengths, $l^* \sim \sqrt{\delta z}$, and $l_c \sim \delta z$ govern the mode structure. A given floppy mode extends over l_c, while the dipolar elastic response has fluctuations which decay over l^*. They argue that a measurement which pins particles on some length scale, like our confined modulus measurement, should be governed by l_c, while one which does not, like our point response measurement, should be governed by l^*. Our results for the confined shear modulus and the transverse piece of the point response are basically consistent with this picture, while our result for the longitudinal piece is inconsistent. For unconstrained deformation of a periodic system, the displacement spectrum would be $S \sim 1/q^2$ by construction within an effective medium approach. We find that this gives the correct baseline behavior but observe deviations from $1/q^2$ which are outside the scope of effective medium approaches.

This opens up several directions for future work. It would be useful to derive an effective medium type scheme which self-consistently accounts for the point response, the spatial structure of response to homogeneous strain, and the values of the global moduli. We should demand that such a scheme account for the distinct behavior of the longitudinal and transverse response and expect this to affect the effective medium estimates for the moduli. One may also wonder if the value of our quoted exponents depends on the range of pressures studied here. Unfortunately, when we decrease ϕ below 0.85, we start to observe finite size effects. This should not be surprising given that we can barely resolve the longitudinal crossover in the point response for $\phi = 0.85$. In the present work, we have worked hard to ensure L remains sufficiently large such that it has no impact in the range of ϕ of interest, spanning a factor of about 100 in pressure. An alternative which should be explored in the future would be to work with more modestly sized systems and analyze the explicit L dependence at lower ϕ. It will also be important to go beyond analysis of two-point correlations. The $u(q)^2 \sim q^2$ scaling arises from local force dipoles (or, equivalently Eshelby transformations). It cannot distinguish between a few strong shear transformations and many weaker ones. The rich structure observed in real space in the strain response are consistent with the 2-point correlations but cannot be determined by them. A more detailed picture – distinguishing between many distributed Eshelby transformations and a few strong ones – will also be crucial going forward to study plasticity, yielding, and steady flow.

Acknowledgments

This material is based upon the work supported by the National Science Foundation under Award Numbers NSF-DMR-1056564 and NSF-CMMI-1250199. We thank Alessio Zaccone for important discussions.

Appendix A: Linear Isotropic Elasticity

The continuum solution $u_\alpha(\mathbf{x})$ is obtained from the equations of motion in terms of the $C_{\alpha\beta\gamma\delta}$ given by [26]

$$(C_{\alpha\beta\gamma\delta} + \mathring{\sigma}_{\beta\delta}\delta_{\alpha\gamma})\partial_\beta\partial_\delta u_\gamma = -f_\alpha, \tag{A1}$$

with f_α being the external body force. We assume that the continuum medium is homogeneous, isotropic, and linearly elastic. The elastic properties of the medium are fully described by the Lamé constants λ and μ, i.e. $C^{\mathcal{L}}_{\alpha\beta\gamma\delta} = \lambda\delta_{\alpha\beta}\delta_{\gamma\delta} + \mu(\delta_{\alpha\delta}\delta_{\beta\gamma} + \delta_{\alpha\gamma}\delta_{\beta\delta})$. Let us also assume that a uniform isotropic initial stress in the reference state is defined by $\mathring{\sigma}_{\alpha\beta} = -p\delta_{\alpha\beta}$ where p is the global pressure. Substituting those expressions into Eq. (A1) yields

$$(\mu - p)\ \partial_\beta\partial_\beta u_\alpha + K\ \partial_\beta\partial_\alpha u_\beta = -f_\alpha, \tag{A2}$$

where $K = \lambda + \mu$ (in $2D$) is the bulk modulus. For a square packing of size L with periodic boundaries along x and y, Eq. (A2) can be solved in terms of a Fourier series

$$u_\alpha(\mathbf{x}) = \sum_{\mathbf{q}} u_\alpha(\mathbf{q})\ e^{i\mathbf{q}.\mathbf{x}}. \tag{A3}$$

Inserting the expansions into Eq. (A2), $u_\alpha(\mathbf{q})$ is most simply displayed as

$$[(\mu - p)\delta_{\alpha\beta} + Kn_\alpha n_\beta]\ u_\beta(\mathbf{q}) = \frac{1}{q^2} f_\alpha(\mathbf{q}), \tag{A4}$$

where $q^2 = q_\alpha q_\alpha$, $n_\alpha = q_\alpha/q$, and $f_\alpha(\mathbf{q}) = \frac{1}{V}\int f_\alpha(\mathbf{x})\ e^{-i\mathbf{q}.\mathbf{x}} dV$.

Given that the longitudinal and transverse waves are the eigenmodes of the Lame-Navier operator – the second order tensor in brackets in Eq. (A4)–, the longitudinal

and transverse components of $u_\alpha(\mathbf{q})$ are

$$u_L^{\rm cont}(\mathbf{q}) = \frac{f_L(\mathbf{q})}{(K+\mu-p)q^2},$$
$$u_T^{\rm cont}(\mathbf{q}) = \frac{f_T(\mathbf{q})}{(\mu-p)q^2}, \quad \text{(A5)}$$

where $f_L(\mathbf{q})$ and $f_T(\mathbf{q})$ are the longitudinal and transverse components of $f_\alpha(\mathbf{q})$, i.e. $f_\alpha(\mathbf{q}) = f_L(\mathbf{q})n_\alpha + f_T(\mathbf{q})n_\alpha^\perp$ where $n_\alpha^\perp n_\alpha = 0$. For a vertical point force of the form $\mathbf{f}(\mathbf{x}) = -F\delta(\mathbf{x})\hat{y}$, the longitudinal and transverse components become

$$f_L(\mathbf{q}) = \frac{F}{V}\sin(\theta),$$
$$f_T(\mathbf{q}) = \frac{F}{V}\cos(\theta), \quad \text{(A6)}$$

where $\delta(\mathbf{x})$ is a delta function, $\hat{y}$ is a unit cartesian vector along y, F is the force magnitude, and θ is the angle of $\mathbf{q}$.

Inserting Eq. (A6) in Eq. (A5) yields

$$u_L^{\rm cont}(\mathbf{q}) = \frac{F\sin(\theta)}{(K+\mu-p)q^2\ V},$$
$$u_T^{\rm cont}(\mathbf{q}) = \frac{F\cos(\theta)}{(\mu-p)q^2\ V}. \quad \text{(A7)}$$

See Appendix B where we derive an expression for K and μ.

Appendix B: Bulk Elastic Constants

Let us now derive microscopic equations for the stress and elastic constants, quantities typically defined from continuum mechanics. Because of the nonaffine displacements, the strain-energy density is now a function of $\delta u_{i\alpha}$ too. Using Eq. (1) and Eq. (9) we have

$$(\mathcal{U}-\mathcal{U}_0)/V \approx \mathring{\sigma}_{\alpha\beta}\eta_{\alpha\beta} + \frac{1}{2}\eta_{\alpha\beta}C_{\alpha\beta\gamma\delta}\eta_{\gamma\delta}, \quad \text{(B1)}$$

where $C_{\alpha\beta\gamma\delta} = C^{\rm Born}_{\alpha\beta\gamma\delta} - \frac{1}{V}\sum_j \Xi^{\alpha\beta}_{i\sigma}H^{-1}_{i\sigma j\tau}\Xi^{\gamma\delta}_{j\tau}$ and $\mathring{\sigma}_{\alpha\beta} = \frac{1}{V}\partial\mathcal{U}/\partial\eta_{\alpha\beta}$. The Born approximation $C^{\rm Born}_{\alpha\beta\gamma\delta}$ for the second derivative of the energy with respect to $\eta_{\alpha\beta}$ corresponds to strictly affine displacements of the particles. The contraction of the inverse of the Hessian on components of $\Xi^{\beta\gamma}_{i\alpha}$ provide the correction terms. Since $H^{-1}_{i\alpha j\beta}$ is positive definite, the correction terms are positive: That is, non-affine displacements *reduce* the second order derivative of the energy from its Born form ($C_{\alpha\beta\gamma\delta} \le C^{\rm Born}_{\alpha\beta\gamma\delta}$ when $\alpha\beta = \gamma\delta$).

In a system with pair-wise interactions, the Born estimates may be computed by carrying out a simple sum over all pairs of interacting particles (see [22])

$$C^{\rm Born}_{\alpha\beta\gamma\delta} = \frac{1}{V}\sum_{ij}[r_{ij}U''(r_{ij}) - U'(r_{ij})]r_{ij}n^\alpha_{ij}n^\beta_{ij}n^\delta_{ij}n^\gamma_{ij} \quad \text{(B2)}$$

where we have introduced the normalized vector between pairs of particles $n^\alpha_{ij} = r^\alpha_{ij}/r_{ij}$. And for the fields $\Xi_{i\alpha\beta\gamma}$, the derived expression is

$$\Xi_{i\alpha\beta\gamma} = -\sum_j [r_{ij}U''(r_{ij}) - U'(r_{ij})]n^\alpha_{ij}n^\beta_{ij}n^\gamma_{ij}. \quad \text{(B3)}$$

Now we are ready to calculate $C_{\alpha\beta\gamma\delta}$ for any particular member of the ensemble. Since we are dealing with large system sizes, we can expect that the quenched stress and elasticity tensors are almost isotropic and C has a form very close to $C^{\mathcal{L}}_{\alpha\beta\gamma\delta}$ (see Appendix A). The two modes of deformation that we need to use here are isotropic compression $\eta_{\alpha\beta} = \epsilon\delta_{\alpha\beta}$ and pure shear $\eta_{\alpha\beta} = \epsilon(\delta_{\alpha x}\delta_{\beta x} - \delta_{\alpha y}\delta_{\beta y})$ where ϵ is an infinitesimal strain. Given these modes of deformation, we are able to make a direct measurements of $K = \frac{1}{4}(C_{xxxx} + C_{yyyy} + 2C_{xxyy})$ and $\mu = \frac{1}{4}(C_{xxxx} + C_{yyyy} - 2C_{xxyy})$.

[1] C. S. O'Hern, L. E. Silbert, A. J. Liu, and S. R. Nagel, Phys. Rev. E **68**, 011306 (2003).
[2] W. G. Ellenbroek, E. Somfai, M. van Hecke, and W. van Saarloos, Phys. Rev. Lett. **97**, 258001 (2006).
[3] W. G. Ellenbroek, M. van Hecke, and W. van Saarloos, Phys. Rev. E **80**, 061307 (2009).
[4] T. G. Mason, J. Bibette, and D. A. Weitz, Phys. Rev. Lett. **75**, 2051 (1995).
[5] M. van Hecke, JOURNAL OF PHYSICS-CONDENSED MATTER **22**, 033101 (2010).
[6] M. Wyart, S. Nagel, and T. Witten, EUROPHYSICS LETTERS **72**, 486 (2005).
[7] M. Wyart, L. Silbert, S. Nagel, and T. Witten, PHYSICAL REVIEW E **72**, (2005).
[8] C. P. Goodrich, W. G. Ellenbroek, and A. J. Liu, SOFT MATTER **9**, 10993 (2013).
[9] S. S. Schoenholz, C. P. Goodrich, O. Kogan, A. J. Liu, and S. R. Nagel, SOFT MATTER **9**, 11000 (2013).
[10] W. G. Ellenbroek, Z. Zeravcic, W. van Saarloos, and M. van Hecke, EPL **87**, (2009).
[11] N. Xu, V. Vitelli, A. J. Liu, and S. R. Nagel, EPL **90**, (2010).
[12] L. Silbert, A. Liu, and S. Nagel, PHYSICAL REVIEW LETTERS **95**, (2005).
[13] E. Lerner, E. DeGiuli, G. During, and M. Wyart, SOFT MATTER **10**, 5085 (2014).

[14] G. During, E. Lerner, and M. Wyart, SOFT MATTER **9**, 146 (2013).
[15] C. E. Maloney, Phys. Rev. Lett. **97**, 035503 (2006).
[16] F. Leonforte, A. Tanguy, J. P. Wittmer, and J.-L. Barrat, Phys. Rev. Lett. **97**, 055501 (2006).
[17] S. Plimpton, Journal of Computational Physics **117**, 1 (1995).
[18] F. Leonforte, A. Tanguy, J. P. Wittmer, and J. L. Barrat, Physical Review B **70**, (2004).
[19] K. Yoshimoto, T. Jain, K. Workum, P. Nealey, and J. de Pablo, Physical Review Letters **93**, (2004).
[20] M. Tsamados, A. Tanguy, C. Goldenberg, and J.-L. Barrat, Physical Review E **80**, (2009).
[21] H. Mizuno, S. Mossa, and J.-L. Barrat, PHYSICAL REVIEW E **87**, (2013).
[22] A. Lemaitre and C. Maloney, Journal of Statistical Physics **123**, 415 (2006).
[23] F. Leonforte, R. Boissiere, A. Tanguy, J. P. Wittmer, and J. L. Barrat, Physical Review B **72**, (2005).
[24] G. Picard, A. Ajdari, F. Lequeux, and L. Bocquet, European Physical Journal E **15**, 371 (2004).
[25] A. J. Liu, S. Ramaswamy, T. G. Mason, H. Gang, and D. A. Weitz, PHYSICAL REVIEW LETTERS **76**, 3017 (1996).
[26] T. H. K. Barron and M. L. Klein, Proceedings of the Physical Society **85**, 523 (1965).
[27] Using the Parseval's theorem, we obtain $\langle \mathbf{u}.\mathbf{u} \rangle = N_g^{-2} \sum_{\mathbf{q}} |u_L(\mathbf{q})|^2 + |u_T(\mathbf{q})|^2$.
[28] Note that $\log |u_T^{\rm cont}(q,\theta)|^2$ is not finite at $\theta = \pi/2$ but the integral over θ is well defined.
[29] Since we are in linear response, there is no difference between dilation and compression other than an overall sign on the displacement and strain field.